CrossMark

JM PAPERS

The fluid dynamics of propagating fronts with solutal and thermal coupling

S. Mukherjee[1] and M.R. Paul[2],†

[1]Department of Mechanical Engineering, University of Minnesota, Minneapolis, MN 55455, USA

[2]Department of Mechanical Engineering, Virginia Tech, Blacksburg, VA 24061, USA

We numerically explore the propagation of reacting fronts in a shallow and horizontal layer of fluid. We focus on fronts that couple with the fluid due to density differences between the products and reactants and also due to heat release from the reaction. We explore fronts where this solutal and thermal coupling is cooperative or antagonistic. We quantify the fluid motion induced by the front and investigate the interactions of the front with the fluid as it propagates through quiescent, cellular and chaotic flow fields. The solutal coupling induces an extended convection roll that travels with the front, the thermal coupling due to heat release from the reaction generates a pair of convection rolls that travels with the front, and when both couplings are present there is a complex signature of these contributions. The details of the front dynamics depend significantly upon the interactions of the front-induced flow field with the fluid ahead of the front.

Key words: buoyancy-driven instability, pattern formation

1. Introduction

A fluid mixture capable of undergoing a process that can be described as an autocatalytic reaction is unstable to a propagating front that consumes reactants and generates products in its wake. In many situations of interest, the front generates fluid motion through its coupling with the fluid. Important coupling mechanisms include buoyancy driven flow due to heat release or absorption by the reaction, and the variation of the density between the products and reactants. If the fluid in which the front is travelling through is not motionless, but is actively stirred, the interactions between the front, the front-induced fluid motion and the bulk fluid motion are coupled with one another, which often results in very rich dynamics and patterns. Many important phenomena can be described as a propagating front in a moving fluid where the dynamics of the front and fluid are coupled. Examples include the dynamics of reacting pollutants in the atmosphere (Jacobson 1999),

† Email address for correspondence: mrp@vt.edu

the spread of a forest fire in the presence of wind (Hargrove *et al.* 2000), combustion in a turbulent flow (Williams 1985; Sreenivasan, Ramshankar & Meneveau 1989), the spread of an epidemic in a moving population (Russell *et al.* 2004) and the complex interactions of reacting chemicals in a stirred aqueous solution (Xin 2000).

We approach this problem from a fundamental point of view rather than with a specific application in mind. We use a reaction–advection–diffusion equation to describe the reaction, which is coupled with a generalized form of the Boussinesq equations for the fluid motion. The precise nature of the coupling between the fluid dynamics and the front depends upon the physical property that is modified by the reaction (cf. De Wit 2020). When the reaction modifies the density of the products we will refer to this as solutal coupling. In this case, the gradient of the density across the front causes buoyancy driven fluid flow in the reaction zone. When the reaction is exothermic, the heat released increases the fluid temperature, which can result in buoyancy driven fluid motion, we will refer to this as thermal coupling. All known autocatalytic reactions are exothermic (Tiani, De Wit & Rongy 2018) and we will only consider this case although our approach is general and endothermic reactions could be explored as well. The dynamics becomes complex when these feedback mechanisms occur simultaneously in a moving fluid.

We explore a propagating front in a horizontal and shallow layer of fluid with solutal and thermal coupling. When solutal and thermal coupling is present, the coupling with the fluid dynamics can be cooperative or antagonistic (cf. D'Hernoncourt, Zebib & De Wit 2007; Rongy & De Wit 2009). The density of the products of an isothermal reaction may be higher, lower or equal to the density of the reactants. The density variation depends upon the particular reaction under consideration. When the products are less dense than the reactants for an exothermic reaction, both mechanisms reduce the density of the fluid in the reaction zone in support of the generation of buoyancy driven flow. In this case, the two coupling mechanisms are cooperative. When the products are more dense than the reactants for an exothermic reaction, these two mechanisms are contrary to one another and the coupling is antagonistic.

The cooperative and antagonistic coupling of propagating autocatalytic fronts has been carefully studied in experiments using closed channels containing aqueous solutions with initially motionless fluid (Pojman & Epstein 1990; Pojman *et al.* 1991*a*; Pojman, Nagy & Epstein 1991*b*; Masere *et al.* 1994; Rongy *et al.* 2009). For horizontal layers of fluid it was demonstrated that any fluid motion induced by the front resulted in an increase in the front velocity. In addition, the presence of solutal coupling resulted in a solutally driven convection roll that encompassed the extended region of space containing the reaction zone, which travelled with the front at the same velocity. For a front travelling from left to right, the solutal convection roll rotates clockwise (counter-clockwise) when the products were less (more) dense than the reactants. Using a Hele-Shaw arrangement, Rongy *et al.* (2009) studied the influence of heat release upon the front and fluid dynamics in the presence of solutal coupling. It was found that the heat release of the reaction distorted the solutal convection roll due to the generation of upflows along the front.

There has been considerable progress on the numerical study of horizontally propagating fronts with coupling through an initially motionless fluid. Vasquez *et al.* (1994) quantified the solutal convection roll in the case without heat release for a two-dimensional layer of fluid with products that are less dense than the reactants. Rongy *et al.* (2007) explored two-dimensional fronts without heat release and with solutal coupling. This was followed by an in-depth numerical investigation of two dimensional fronts with cooperative and antagonistic coupling (Rongy *et al.* 2009; Rongy & De Wit 2009). The studies by Rongy *et al.* (2007, 2009) and Rongy & De Wit (2009) assumed

Stokes flow for an aqueous solution with third-order reaction kinetics in a shallow layer bounded above and below by perfectly insulating no-slip surfaces. This work quantified the increased front velocity and mixing length of fronts with coupling as well as elucidated the symmetry properties of the front shape for a wide range of conditions. Jarrige *et al.* (2010) used the two-dimensional gap-averaged equations to quantify the scaling behaviour of the front velocity and mixing length with system parameters for fronts propagating in Hele-Shaw cells.

The front and fluid dynamics can become very complicated for fronts propagating through a moving fluid. In the absence of heat release from the reaction and without solutal coupling, it has been found that two-dimensional cellular flow, in the form of a chain of vortices, enhances the front propagation (Abel *et al.* 2001, 2002; Pomeau 2004; Pocheau & Harambat 2008). Experimental studies have probed the dynamics of reacting fronts in a moving fluid for a diverse range of conditions including disordered vortex flows (Bargteil & Solomon 2012; Nevins & Kelley 2016), blinking vortex flows (Nugent, Quarles & Solomon 2004) and disordered cellular flows with a wind (Schwartz & Solomon 2008).

A systematic numerical study was performed of the propagation of a three-dimensional front through cellular, chaotic and weakly turbulent flow fields by Mehrvarzi & Paul (2014) and Mukherjee & Paul (2019). It was found that the disordered flow fields, in general, increased the geometric complexity of the front and resulted in a fractal geometry when measured using the box counting dimension. The front velocity was found to depend in a subtle way upon the orientation of the bulk convective flow field relative to the direction of propagation of the front. As the flow complexity increased, with the introduction of smaller scale features in the flow field, the front velocity increased. Mukherjee & Paul (2020) conducted a detailed study of the propagation of a front through a cellular flow field with solutal coupling and without heat release by the reaction. The scaling properties of the front-induced fluid velocity, front velocity and mixing length were determined for a wide range of parameters. The interactions between the propagating front, the front induced fluid velocity composing the solutal convection roll and the cellular flow were quantified to reveal very complex spatio-temporal features. In the studies by Mehrvarzi & Paul (2014) and Mukherjee & Paul (2019, 2020) the cellular, chaotic and weakly turbulent flow fields were generated by imposing a constant temperature difference between the bottom and top bounding surfaces of the fluid domain resulting in Rayleigh–Bénard convection. In the research described here, we present results for the much more difficult, and realistic, case of a fully coupled front propagating through complex flow fields generated by Rayleigh–Bénard convection.

The remainder of the paper is organized as follows. In § 2 we discuss the governing equations, important non-dimensional parameters and our overall numerical approach. In § 3 we discuss the results of our investigation. We begin in § 3.1 by quantifying the fluid and front dynamics of an exothermic front, without any additional forms of coupling, that is, propagating through a quiescent two-dimensional layer of fluid. We use this study to build a baseline of understanding. In § 3.2 we include solutal coupling and in § 3.3 we include a cellular flow field driven by thermal convection. We next explore the complex dynamics of fronts propagating through a three-dimensional chaotic fluid layer in § 3.4. Lastly, we present our concluding remarks in § 4.

2. Approach

The most general situation we consider is the propagation of an exothermic front with solutal coupling in a shallow horizontal layer of fluid that is undergoing thermal convection. We will use this case to introduce the governing differential equations.

The conservation of momentum, energy and mass of the fluid can be expressed in non-dimensional form as

$$Pr^{-1} \left(\frac{\partial \boldsymbol{u}}{\partial t} + \boldsymbol{u} \cdot \boldsymbol{\nabla} \boldsymbol{u} \right) = -\boldsymbol{\nabla} p + \nabla^2 \boldsymbol{u} + Ra_T T \hat{z} + Ra_s c \hat{z}, \tag{2.1}$$

$$\frac{\partial T}{\partial t} + \boldsymbol{u} \cdot \boldsymbol{\nabla} T = \nabla^2 T + \eta f(c), \tag{2.2}$$

$$\boldsymbol{\nabla} \cdot \boldsymbol{u} = 0, \tag{2.3}$$

where $\boldsymbol{u}$ is the fluid velocity vector, p is the pressure, T is the temperature, c is the concentration of the products, $\hat{z}$ is a unit vector opposing gravity and $f(c)$ is a nonlinear function of c describing the heat release of the exothermic reaction. The variation of the concentration is governed by the reaction–advection–diffusion equation given by

$$\frac{\partial c}{\partial t} + \boldsymbol{u} \cdot \boldsymbol{\nabla} c = Le \nabla^2 c + \xi f(c). \tag{2.4}$$

Equations (2.1)–(2.4) are non-dimensionalized using the depth of the fluid layer, d, as the length scale and the vertical diffusion time of heat, $\tau_\alpha = d^2/\alpha$, as the time scale, where α is the thermal diffusivity of the fluid, τ_α is the time scale for heat to diffuse from the bottom to the top of the fluid layer. The constant temperature difference between the bottom and top walls, ΔT, is used as the temperature scale, which yields $T(z = 0) = 1$ and $T(z = 1) = 0$. We note that the constant temperature boundary conditions indicate that the bottom and top surfaces are perfect thermal conductors. The initial concentration of reactants, a_0, is used as the concentration scale. As a result, $0 \le c \le 1$ where $c = 1$ is pure products and $c = 0$ is pure reactants. A typical definition of a front is the isocontour where $c = 1/2$ and the reaction zone is the spatial region where $0 < c < 1$.

There are several important non-dimensional parameters in (2.1)–(2.4). The Prandtl number, $Pr = \nu/\alpha$, is the ratio of the momentum and thermal diffusivities where ν is the kinematic viscosity of the fluid. In our results, we use $Pr = 1$, which is aligned with typical Rayleigh–Bénard convection experiments using compressed gases to study the state of spiral defect chaos (Morris *et al.* 1993; Bodenschatz, Pesch & Ahlers 2000). A Prandtl number of $Pr \approx 7$ would be required to describe front propagation in an aqueous medium. However, spiral defect chaos is quenched for increased values of the Prandtl number (Chiam *et al.* 2003). Our intention is not to quantitatively describe an aqueous reaction but rather to carefully study the coupling between a front and a complex fluid flow.

There are two Rayleigh numbers that are needed to describe this problem. The thermal Rayleigh number, $Ra_T = \beta_T g \Delta T d^3/(\alpha \nu)$, is the ratio of buoyancy caused by temperature variations to viscous dissipation where β_T is the thermal expansion coefficient. For an infinite layer of fluid with no-slip boundaries the critical Rayleigh number marking the onset of convection is $Ra_{T,c} \simeq 1708$ (Chandrasekhar 1961). The solutal Rayleigh number, $Ra_s = \beta_s g a_0 d^3/(\alpha \nu)$, is the ratio of buoyancy caused by concentration variations to viscous dissipation where β_s is the solutal expansion coefficient. A positive (negative) value of Ra_s indicates that the products of the reaction are less (more) dense than the reactants. Any non-zero value of Ra_s will induce fluid motion.

The Lewis number, Le, is the ratio of mass diffusion to heat diffusion $Le = D/\alpha$, where D is the coefficient of molecular diffusion of the autocatalytic product. Smaller values of the Lewis number, $Le < 1$, imply a stronger influence of the fluid flow on the front dynamics. We will use $Le = 0.01$ in our two-dimensional study and $Le = 0.1$

in our three-dimensional study where the computations are much more demanding. The non-dimensional reaction rate, $\xi = \tau_\alpha/\tau_r$, is a ratio of time scales where τ_r is the reaction time scale defined as $\tau_r = (k_r a_0)^{-1}$ and k_r is the dimensional reaction rate. We use a value of $\xi = 9$. Our choices of Le and ξ are motivated by our interest to study fronts where the time scale of the fluid motion is comparable to the reaction time scale while being smaller than the time scale of molecular diffusion. As a result, in our study we have fronts of finite thickness where convective fluid motion plays a significant role in the front dynamics.

The heat release parameter, η, is defined as $\eta = -\xi \Delta H/(\rho_0 c_p \Delta T)$ where c_p is the specific heat capacity of the fluid, ρ_0 is the reference density and ΔH is the enthalpy change due to the reaction. Any non-zero value of η induces fluid flow and for exothermic reactions $\Delta H < 0$, which yields $\eta > 0$. We use values of η such that the maximum temperature in the domain remains of the order of unity.

We use the Fisher–Kolmogorov–Petrovskii–Piskunov (FKPP) nonlinearity (Fisher 1937; Kolmogorov, Petrovskii & Piskunov 1937) as the production term for the reaction which can be expressed as $f(c) = c(1 - c)$. The FKPP nonlinearity has been used to model a wide range of problems such as radial chain branching, bimolecular chemical reactions and the Belousov–Zhabotinsky reaction (Field & Burger 1985; Wu *et al.* 1995; van Saarloos 2003). Propagating fronts generated by the FKPP reaction that are coupled with convective fluid flow have been studied in Mehrvarzi & Paul (2014), Mukherjee & Paul (2019, 2020) and Abel *et al.* (2001, 2002).

We use the no-slip boundary condition $\boldsymbol{u} = 0$ on all the material surfaces. The lateral sidewalls are assumed to be perfect thermal conductors, which yields a linear conduction temperature profile of $T(z) = 1 - z$ at these boundaries. The temperature at the bottom surface is $T(z = 0) = 1$ and the temperature of the top surface is $T(z = 1) = 0$. The boundary condition for the concentration at all material surfaces is the no-flux condition, $\nabla c \cdot \hat{n} = 0$, where $\hat{n}$ is an outward pointing unit normal.

Figure 1 shows the two-dimensional and three-dimensional domains used in our numerical simulations. For the two-dimensional domain, the aspect ratio is $\Gamma = L_x/d = 30$, where L_x is the length of the fluid layer. The front is initiated at the left wall, which then propagates to the right. For the three-dimensional cylindrical domain, the aspect ratio is $\Gamma = r_0/d = 40$ where r_0 is the radius of the domain. In this case, the front is initiated at the centre of the domain, which then propagates radially outward.

The initial conditions for the fluid depend upon the case under consideration. For fronts propagating through an initially quiescent layer of fluid we set $Ra_T < Ra_{T,c}$. In this case, the fluid is initially motionless everywhere such that $\boldsymbol{u}(t = 0) = 0$ while the temperature of the fluid in the layer is initially given by the linear conduction profile, $T(t = 0) = 1 - z$. The linear temperature profile is the steady state solution of (2.2) in the absence of a reaction when the thermal Rayleigh number is below critical.

For fronts propagating through a complex flow field generated by Rayleigh–Bénard convection we first conduct a long-time simulation of the fluid equations in the absence of the reaction to establish the flow field. When initializing a simulation to establish a convective flow field, we set $Ra_T > Ra_{T,c}$ with an initial fluid velocity of zero everywhere with small random perturbations to the temperature field. We use an initial concentration field that decays exponentially in space. In the two-dimensional domain we use $c(x, z, t = 0) = \exp(-(\xi/Le)^{1/2}x)$ and in the three-dimensional domain we use $c(x, y, z, t = 0) = \exp(-2(x^2 + y^2))$. We have confirmed that fronts initiated from these initial conditions, in a quiescent fluid, have a front speed v_0 that is in agreement with the theoretical prediction of $v_0 = 2\sqrt{Le\xi}$ for a pulled front (van Saarloos 2003). A detailed exploration of fronts
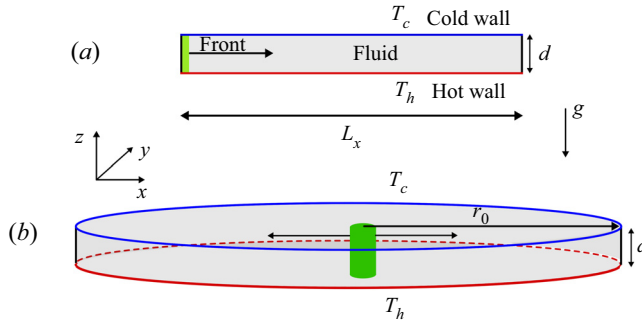
Figure 1. The (*a*) two-dimensional and (*b*) three-dimensional domains used to study front propagation in a horizontal layer of fluid. Cartesian coordinates (x, y, z) are shown with gravity g opposing the z-direction. The bottom surface is hot (red) at T_h, the top surface is cold (blue) at T_c and the depth of the fluid layer is d. (*a*) For the rectangular domain, $\Gamma = L_x/d$, where L_x is the length of the domain and $\Gamma = 30$ in our study. The front is initiated at the left wall (green) and travels to the right. (*b*) For the cylindrical domain, $\Gamma = r_0/d$, where r_0 is the radius of the domain and $\Gamma = 40$ in our study. The front is initialized at the centre (green) and propagates radially outward. The domains are not drawn to scale.

through a quiescent fluid without solutal and thermal coupling is given in Mukherjee & Paul (2019).

We use the open source spectral element fluid solver Nek5000 (Fischer 1997; Deville, Fischer & Mund 2002; see https://nek5000.mcs.anl.gov) to integrate (2.1)–(2.4). For the two-dimensional domain we use 480 equally sized square spectral elements. For the three-dimensional cylindrical domain we use 3072 hexahedral spectral elements. For spatial discretization we use 16th-order Lagrangian interpolant polynomials. The time stepping is third-order accurate and uses an operator splitting approach. We have conducted detailed spatial and temporal resolution tests to verify our computations, more details can be found in Mukherjee (2020). This numerical approach has been used to study propagating fronts for a broad range of conditions in Mehrvarzi & Paul (2014) and Mukherjee & Paul (2019, 2020).

3. Results and discussion

We quantify the interactions of the front and fluid as a function of the heat release of the reaction, the density variation between the products and reactants due to the reaction, and the complexity of an imposed flow field. In order to isolate these different contributions we hold constant the values of all parameters except for Ra_T, Ra_s and η. It is within this space of parameters that we have conducted our investigation.

We begin by focusing on the case of a two-dimensional layer of fluid. We first study an exothermic front propagating through an initially quiescent fluid where the products and reactants have the same density. In terms of the non-dimensional parameters, this yields $Ra_T < Ra_{T,c}$, $Ra_s = 0$ and $\eta > 0$. We then only vary η to quantify the effect of heat release on the fluid flow generated by the front. We next include solutal effects ($Ra_T < Ra_{T,c}$, $Ra_s \neq 0$, $\eta > 0$). This allows us to study fronts with cooperative and antagonistic feedback in an initially motionless fluid. We next include a flow field generated by Rayleigh–Bénard convection to investigate exothermic fronts with solutal coupling in a cellular flow field ($Ra_T > Ra_{T,c}$, $Ra_s \neq 0$, $\eta > 0$). We then explore fronts in the three-dimensional cylindrical domain that propagate through a spatio-temporally chaotic flow field driven by Rayleigh–Bénard convection ($Ra_T > Ra_{T,c}$, $Ra_s \neq 0$, $\eta > 0$).
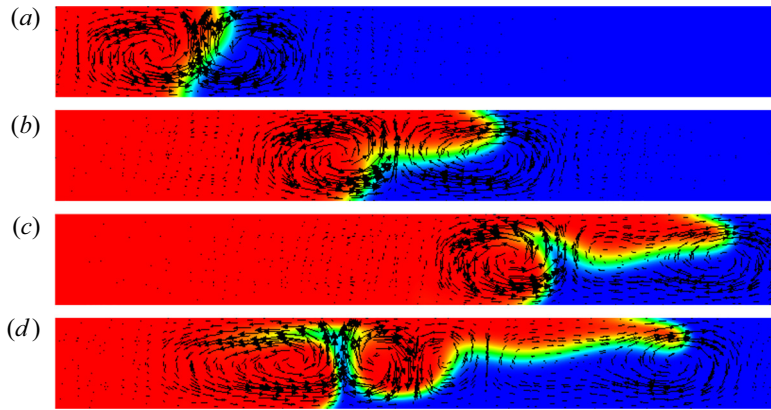
Figure 2. Exothermic fronts without solutal coupling propagating through a quiescent fluid ($Ra_T = 1000$, $Ra_s = 0$, $\eta > 0$). Colour contours of $c(x, z, t)$, where red is pure products and blue is pure reactants. Arrows are fluid velocity vectors; (*a*) $\eta = 1$, (*b*) $\eta = 10$, (*c*) $\eta = 20$, (*d*) $\eta = 50$. All images are at time $t = 6$ where the fronts were initiated at $t = 0$. A zoomed-in view is shown to illustrate the front features: (*a–c*) show $2 \le x \le 10$ and (*d*) shows $8 \le x \le 16$. The maximum values of fluid velocity magnitudes present in (*a–d*) are 0.13, 1.08, 2.09 and 3.85.

3.1. *An exothermic front in a quiescent fluid ($Ra_T < Ra_{T,c}$, $Ra_s = 0$, $\eta > 0$)*

Our first investigation provides insight into the fluid and front dynamics resulting from the propagation of an exothermic front in the absence of additional complexities such as solutal coupling or an externally driven flow field. This provides an important baseline understanding that will be useful in our subsequent studies when more complex couplings are present. We consider an exothermic front, $\eta > 0$, propagating in a two-dimensional horizontal layer of an initially quiescent fluid, $Ra_T < Ra_{T,c}$, without solutal effects $Ra_s = 0$. The geometry used is shown in figure 1(*a*). Specifically, we use $Ra_T = 1000$ while varying η over the range $1 \le \eta \le 100$. For these conditions, all fluid motion is caused by the heat release from the reaction. This generates a region of front-induced fluid motion that travels with the front and, after the front has passed, the fluid will return to a motionless state.

Figure 2 shows fronts for several values of η where η increases from (*a–d*), respectively. The fronts are travelling from left to right and the colour contours are of $c(x, z, t)$ where blue is pure reactants, red is pure products and the yellow–green region is the reaction zone. The finite width of the reaction zone is clearly evident. Fluid velocity vectors are shown by the black arrows, which illustrate the complex fluid motion generated in the region near the front. Figure 2(*a–c*) shows a close-up view of a portion of the domain, $2 \le x \le 10$, to highlight the front details. Figure 2(*d*) is for $\eta = 50$, which results in a much faster front and the portion shown is $8 \le x \le 16$. All fronts are shown at $t = 6$ where the front initiation occurs at $t = 0$. As a result, insight into the front velocity can be gained by the relative position of the fronts in figure 2(*a–c*), which indicates an increasing front speed with increasing η, as expected.

For small and intermediate values of the heat release parameter, $\eta \lesssim 20$, which corresponds to figure 2(*a–c*), the front generates a pair of counter-rotating convection rolls that travel with the front and encompass the entire reaction zone (the region spanned in the x-direction by the yellow/green contours). Between the two convection rolls is an upflow due to the heat release of the reaction, which reduces the fluid density due to increased temperature. Fluid heated by the reaction within the reaction zone rises buoyantly toward
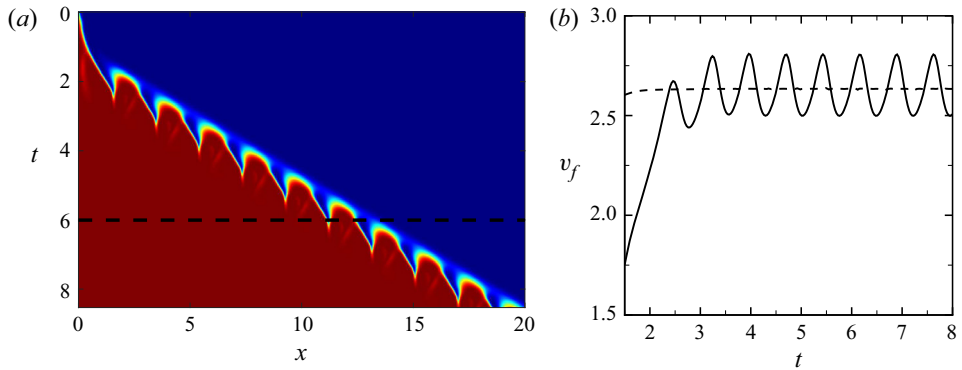
Figure 3. The spatio-temporal dynamics of an exothermic front without solutal coupling propagating through an initially motionless fluid ($Ra_T = 1000$, $Ra_s = 0$, $\eta = 50$). (*a*) Space–time plot of $c(x, z = 1/2, t)$, where red is products and blue is reactants. (*b*) The front velocity (solid line) as a function of time using the bulk-burning rate approach, see (3.1). The dashed line is the velocity of the leading edge of the front computed using a front-tracking approach.

the top wall. The fluid cools as it interacts with the cold top wall, which increases its density eventually causing it to fall. As η increases, the magnitude of the fluid velocity, front velocity and mixing length increase. This causes the clockwise rotating convection roll (the right roll of the pair) to extend laterally toward larger values of x as the front extends and deforms. As the magnitude of the upflow between the pair of convection rolls increases, reactants are advected vertically, creating a cusp-like feature in the front. The cusp is particularly striking in figure 2(*c–d*). The upflow draws in reactants which can yield isolated regions of reactants that become surrounded by products. These islands of reactants are rapidly consumed by the reaction. This event repeats periodically and results in a time dependence for the cusp region (see supplementary movie 1 available at https://doi.org/10.1017/jfm.2022.375). We point out that this flow field is quite different than what occurs when only solutal coupling is included, which results in a single large convection roll that travels with the front (for example, see figure 2 of Mukherjee & Paul 2020).

Overall, the complexity of the front increases with increasing values of η. In figure 2(*d*) the cusp structure extends upward nearly to the top wall and the leading edge of the front is stretched considerably toward the right. The right convection roll of the roll pair created by the exothermic reaction no longer extends far to the right. A second pair of convection rolls has been formed on its right side, which results in the formation of a second smaller cusp feature. The leading edge of the front extends over the top regions of these convection rolls to yield a very stretched structure.

The spatio-temporal dynamics of the front for $\eta = 50$ is further illustrated by the space–time plot of figure 3(*a*), where we show colour contours of $c(x, z = 1/2, t)$ as a function of x and t. Red regions are pure products and blue regions are pure reactants. We have found that the mid-plane slice is insightful since it captures features that extend into the bulk of the fluid layer. Other choices of z could be used to emphasize different dynamical features of the fronts if desired. The rounded peak features (red) are the first to complete the reaction. These peaked regions coincide with the initial formation of the cusp structure and the bottoms of the sharp trough regions (blue) coincide with the fully formed cusp. The horizontal dashed line at $t = 6$ coincides with the front shown in figure 2(*d*) where the cusp structure is nearly fully formed.

The variation for the front velocity with time is shown in figure 3(*b*). The solid line is $v_f(t)$ when computed using the bulk-burning rate approach (Constantin *et al.* 2000) where

$$v_f(t) = \int_0^1 dz \int_0^\Gamma \frac{dc}{dt} dx. \tag{3.1}$$

The bulk-burning rate is advantageous because it remains valid for complicated fronts, such as these, where front-tracking approaches can be difficult to implement and compute (Mukherjee & Paul 2019, 2020). An important feature of the bulk-burning rate approach is that it accounts for the front dynamics over the entire reaction zone, and not only a particular region that is tracked. For this front, the bulk-burning rate approach includes the region containing the dynamics of the cusp. It is insightful to compare $v_f(t)$ with the velocity of the leading edge of the front (the portion of the front furthest to the right) using a simple front-tracking approach. The velocity of the leading edge is shown by the dashed line, which reaches a steady value. This is in contrast to the time periodic front velocity shown by the solid line. The time average of $v_f(t)$ equals that of the leading edge for $t \gtrsim 4$. We will find the bulk-burning rate approach to determining the front velocity useful as we quantify more complex fronts.

The variation of the temperature field can be used to gain more insight into the dynamics of an exothermic front. The variation of $T(x, z, t)$ is shown in figure 4 for different values of η, where red is hot fluid and blue is cold. Fluid velocity vectors are shown using arrows and the front location is indicated by including the $c = 1/2$ contour as a solid black line. Away from the reaction zone, where there is no fluid motion, the conduction temperature profile is evident by the linear transition from red to blue. For small values of heat release, such as figure 4(*a*), where $\eta = 1$, a small deviation from the linear temperature profile is evident at the upflow region in between the counter-rotating convection rolls. The front has also developed some curvature. For larger values of η, the deviation from the linear profile increases significantly and the shape of the front becomes more complex. As the front extends laterally for larger values of η, the region of heated fluid also increases as expected.

The maximum temperature in the fluid layer for $\eta \lesssim 20$ is at the hot bottom wall. For larger values of η the maximum temperature is away from the wall and is in the region where the front forms a cusp. For an exothermic reaction coupled to the flow field using the FKPP nonlinearity, as shown in (2.2), the production term $\eta c(1 - c)$ is at the maximum at $c = 1/2$. The front forms a fold in the region near the cusp, which results in a significant spatial region where $c \approx 1/2$. Therefore, in the cusp region there is significant heat release. Moreover, this is also the region with the strongest upflow, which draws in fresh reactants. Both of these effects combine to form a hotspot in the cusp region of the fluid. Once the reaction is completed in the cusp region, the front continues its advance to form another cusp and hot spot and the dynamical process repeats.

We next quantify the characteristic fluid velocity U, the front velocity v_f and the mixing length L_s as a function of the heat release η. For U we use the maximum value of the fluid velocity in the domain. Here, v_f is computed using (3.1) and L_s is a measure of the width of the reaction zone and it is defined as the spatial extent in the *x*-direction over which the depth-averaged value of the concentration field is in the range $0.01 \leq \langle c(x, t) \rangle \leq 0.99$, where the angle brackets indicate the depth average (Rongy *et al.* 2007; Rongy & De Wit 2009). All three of these measures are functions of time and they grow until reaching steady conditions for $t \gtrsim 4$. For larger values of the heat release, $\eta \gtrsim 10$, all of the measures display oscillations of magnitude $O(10^{-1})$ around a mean value that represents
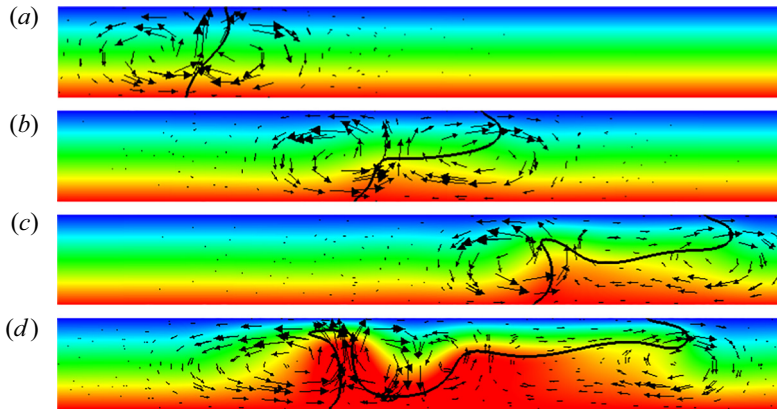
Figure 4. The variation of the fluid temperature for an exothermic front propagating though an initially motionless fluid, where (*a*) $\eta = 1$, (*b*) $\eta = 10$, (*c*) $\eta = 20$, (*d*) $\eta = 50$. Colour contours of $T(x, z, t)$, where red is hot fluid and blue is cold fluid. Arrows indicate fluid velocity vectors and the solid line is the isocontour at $c = 1/2$ indicating the location of the front. The concentration fields for these fronts are shown in figure 2. All images are at $t = 6$. For (*a–c*) the maximum temperature is $T = 1$ and for (*d*) it is $T \gtrsim 1$ due to the strong exothermic reaction. Remaining parameters: $Ra_T = 1000$, $Ra_s = 0$.

its time-averaged value. The mean values of the characteristic velocity, front velocity and mixing length will be denoted as $\bar{U}$, $\bar{v}_f$ and $\bar{L}_s$.

The variations of $\bar{U}$, $\bar{v}_f$ and $\bar{L}_s$ with η are shown in figure 5, which reveals that all of these quantities monotonically increase with the amount of heat release. The trends in the data further suggest the presence of different regimes based upon the value of η. In light of this, we have divided the results into small, intermediate and large values of η. We use the following conventions in the figures: small η is $0 \leq \eta \leq 1$ and uses circles (blue); intermediate η is $1 < \eta \leq 20$ and uses diamonds (green); and large values of η is $\eta > 20$ and uses squares (red). We find that small and large values of η are described well using scaling relationships and the intermediate values of η appear to represent a transition region.

Figure 5(*a*) shows the variation of $\bar{U}$ with η. For small η, $\bar{U}$ varies linearly with η, as indicated by the solid line, which is a curve fit of the form $\bar{U} = 0.127\eta$. For large η, U follows a square root scaling as indicated by the dashed line representing $\bar{U} = 0.465\eta^{1/2}$. For intermediate values of η the trend suggests a transition between these two regimes of small and large heat release. A similar trend is observed for propagating fronts with only solutal feedback ($Ra_s \neq 0$, $\eta = 0$, $Ra_T < Ra_{T,c}$), where $\bar{U}$ varies linearly for small values of Ra_s and transitions to square root scaling for large values of Ra_s although the flow structure for purely solutal feedback is a single convection roll that travels with the front (Mukherjee & Paul 2020).

The variation of $\bar{v}_f$ with η is shown in figure 5(*b*). The front velocity is normalized by $v_0 = 2\sqrt{Le\xi}$, which represents the analytical result for the front velocity of a pure reaction diffusion system with FKPP kinetics (Kolmogorov *et al.* 1937). For our parameters this yields $v_0 = 0.6$, which represents a useful baseline value for comparison. For small η, the front velocity scales as $\eta^{3/2}$ where the solid line is the curve fit $(\bar{v}_f - v_0)/v_0 = 0.151\eta^{3/2}$. For large η, the front velocity transitions to a $\eta^{1/2}$ scaling where the dashed line is the curve fit $(\bar{v}_f - v_0)/v_0 = 0.503\eta^{1/2}$. The data in the transition regime are shown using the green diamonds.
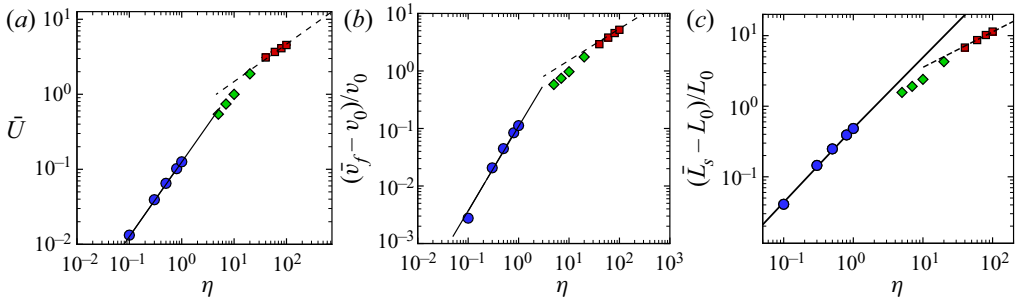
Figure 5. The variation of the asymptotic fluid velocity $\bar{U}$, front velocity $\bar{v}_f$ and mixing length $\bar{L}_s$ with η for an exothermic front in a quiescent fluid ($Ra_T = 1000$, $Ra_s = 0$, $\eta > 0$). Small, intermediate and large values of η are represented using circles (blue), diamonds (green) and squares (red), respectively. (*a*) The variation of $\bar{U}$ with η. The solid line is $\bar{U} = 0.127\eta$ and the dashed line is $\bar{U} = 0.465\eta^{1/2}$. (*b*) The variation of the front velocity with η, where $v_0 = 0.6$ is the analytical front velocity for $\eta = 0$. The solid line is $(\bar{v}_f - v_0)/v_0 = 0.151\eta^{3/2}$ and the dashed line is $(\bar{v}_f - v_0)/v_0 = 0.503\eta^{1/2}$. (*c*) The variation of the mixing length with η, where $L_0 = 0.6$ is the analytical mixing length for $\eta = 0$. The solid line is $(\bar{L}_s - L_0)/L_0 = 0.49\eta$ and the dashed line is $(\bar{L}_s - L_0)/L_0 = 1.127\eta^{1/2}$.

Figure 5(*c*) shows the variation of $\bar{L}_s$ with η. The mixing length is normalized by the mixing length of a pure reaction diffusion front where $L_0 = 0.6$. The mixing length follows the same scaling trends as the characteristic fluid velocity. For small η, the mixing length increases linearly with increasing η where the solid line is the curve fit $(\bar{L}_s - L_0)/L_0 = 0.49\eta$. For large values of η, the square root dependence is shown by the dashed line which is the curve fit $(\bar{L}_s - L_0)/L_0 = 1.127\eta^{1/2}$. The green diamonds again indicate a transition region between the scaling regimes found for small and large η.

3.2. *An exothermic front with solutal feedback in a quiescent fluid* ($Ra_T < Ra_{T,c}$, $Ra_s \neq 0$, $\eta > 0$)

We now consider the propagation of an exothermic front where the products and reactants have different densities in an initially motionless layer of fluid. We set $Ra_T = 1000$ and $\eta = 50$ and explore how the front dynamics varies with Ra_s. For these conditions, the presence of cooperative or antagonistic feedback will depend upon the sign of Ra_s. When $Ra_s > 0$, the products are less dense than the reactants, and this yields cooperative feedback since both the heat release and the density change due to the reaction are enhancing buoyant convection. When $Ra_s < 0$, the products are more dense than the reactants, and this yields antagonistic feedback because the solutal changes reduce buoyant convection while the exothermic reaction is enhancing buoyant convection. We explore a cooperative case where $Ra_s = 300$, and an antagonistic case where $Ra_s = -300$.

Figure 6 shows the fluid and front dynamics for (*a*) cooperative feedback and (*b*) antagonistic feedback using the plotting conventions of figure 2. In the cooperative case, the combined result of the solutal and thermal coupling yields a significantly extended leading edge of the front. The velocity of the leading edge of the front is steady in time. The extended leading edge of the front in figure 6(*a*) is coincident with a large clockwise convection roll that has been induced by the front. For $Ra_s > 0$, solutal coupling alone will generate a large clockwise convection roll that propagates with an extended front (cf. Rongy *et al.* 2007; Mukherjee & Paul 2020). Also, for $\eta > 0$, the heat release from the reaction generates a convection roll with clockwise rotation that travels with the leading edge of the front, as shown in figure 2(*d*). Therefore, in the case we are exploring
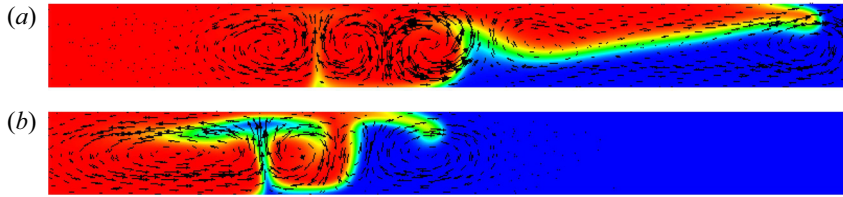
(*a*)

(*b*)

Figure 6. Exothermic fronts with solutal feedback propagating through an initially motionless layer of fluid. Colour contours of $c(x, z, t)$, where blue is pure reactants and red is pure products. Arrows are fluid velocity vectors. (*a*) Cooperative feedback: $Ra_T = 1000$, $Ra_s = 300$, $\eta = 50$. (*b*) Antagonistic feedback: $Ra_T = 1000$, $Ra_s = -300$, $\eta = 50$. The images are at $t = 5.97$ and a close-up view is shown for $8 \leq x \leq 17$. The characteristic fluid velocities are (*a*) $U = 3.84$ and (*b*) $U = 3.67$.

here with $Ra_s > 0$ and $\eta > 0$, both of these effects contribute to the large clockwise convection roll that propagates with the leading edge on the right side of figure 6(*a*).

The extended leading edge of the front is followed, on its left side, by a dynamic cusp structure. The cusp structure can be identified as the region where the reactants extend further toward the top wall than in its immediate surroundings due to the upflow between two counter-rotating convection rolls. The dynamics of the cusp region is similar to what we found for an exothermic front without solutal feedback, for example see figure 2(*d*). As a result, we attribute this to the heat release from the reaction. The reactants inside the cusp are rapidly consumed and, as the front advances, these cusp structures are periodically formed. The cusps again contain a hotspot where the temperature of the fluid layer is at its maximum. It is interesting to note that Rongy & De Wit (2009) found that horizontally propagating cooperative fronts have a hotspot behind the front located at the bottom plate. In addition to exploring a different parameter regime than we do here for a cubic autocatalytic reaction kinetics, Rongy & De Wit (2009) also used thermally insulating boundary conditions at the top and bottom plates where the only source of heat was the exothermic reaction. This boundary condition is different from the problem we have studied where the top and bottom plates are perfect thermal conductors that are maintained at a constant temperature difference.

Figure 6(*b*) shows the fluid and front dynamics for antagonistic feedback. In this case, the spatial structure and dynamics of the leading edge of the front are significantly different. The leading edge of the front is again coincident with a convection roll of clockwise rotation. For solutal coupling alone with $Ra_s < 0$, the front generates a large extended surface that is coincident with a counter-clockwise convection roll (Rongy *et al.* 2007), which is contrary to the clockwise convection roll at the leading edge that is generated by the heat release. For the parameters we have used, $\eta = 50$ is large enough such that the resulting convection roll when both feedback mechanisms are present is of clockwise rotation even though $Ra_s < 0$ as shown in figure 6(*b*). Since the products of the exothermic reaction are more dense than the reactants, the leading edge extends only a short distance before falling down under the influence of gravity. During this motion, the leading edge traps fresh lighter reactants which are rapidly consumed. This is followed, to the left, by the pair of convection rolls generated by the exothermic reaction. The upflow between these rolls draws in fresh reactants to generate a plume structure containing reactants. The plume containing reactants is lighter than the surrounding products and extends nearly to the top wall before extending laterally. The isolated reactants are quickly consumed and the entire process repeats. This periodic rolling and tumbling motion of the leading edge has been observed experimentally (Nagypal, Bazsa & Epstein 1986; Rongy & De Wit 2009; Rongy *et al.* 2009). Chemical oscillations and time varying
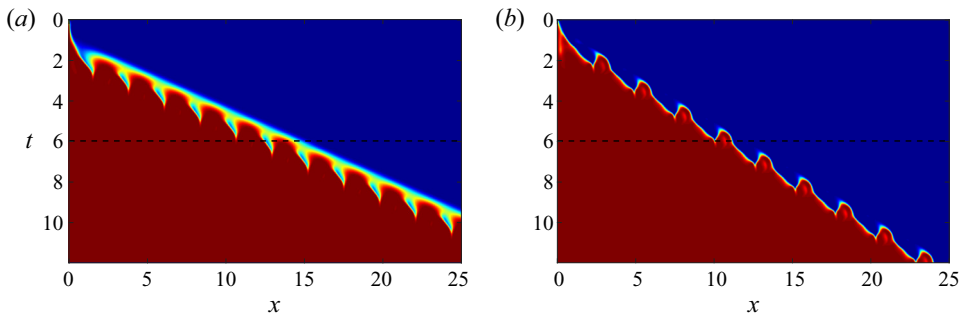
Figure 7. Space–time plots of fronts with (*a*) cooperative feedback and (*b*) antagonistic feedback through an initially motionless fluid. Colour contours of $c(x, z = 1/2, t)$, where red is pure products and blue is pure reactants. (*a*) Cooperative feedback: $Ra_T = 1000$, $Ra_s = 300$, $\eta = 50$. (*b*) Antagonistic feedback: $Ra_T = 1000$, $Ra_s = -300$, $\eta = 50$. Front images at $t = 5.97$ (dashed line) are shown in figure 6.

convective dynamics have also been explored in detail for reactions with antagonistic coupling between solutal and surface tension contributions (Budroni, Rongy & De Wit 2012; Budroni, Upadhyay & Rongy 2019).

Figure 7 shows space–time plots of the fronts with (*a*) cooperative feedback and (*b*) antagonistic feedback, where red is pure products and blue is pure reactants. The reaction zone is located along the yellow–green region that extends from the upper left corner to the lower right corner. The slope of a line fitted along the reaction zone would yield an estimate of the inverse of the front velocity. It is evident from figure 7 that the front with cooperative feedback has a larger front velocity than the front with antagonistic feedback. The space–time plots also indicate clear differences in the front dynamics for these two cases, which we now discuss in more detail.

Figure 7(*a*) shows the space–time plot for the front with cooperative feedback. The extended leading edge of the front is steady in time and yields the linear shape on the right-hand side of the reaction zone. In the absence of solutal or thermal feedback, the front propagates with a constant velocity, which would yield a solid yellow–green line from the upper left to the lower right of the space–time plot, as shown in Mukherjee & Paul (2020). However, the space–time plot of figure 7 shows repeating features in the reaction zone. These features are comprised of rounded peaks of products followed by troughs containing reactants. In a reference frame moving with the front, these repeating features represent the time-periodic dynamics that results from the cooperative coupling that is present. These repeating features are a result of the periodic dynamics of the cusp structure that is driven by the heat release from the reaction. A horizontal slice of the space–time plot would reveal the complex transition from products to reactants that occurs as a function of distance in the x direction at that particular time. The dashed line at $t = 5.97$ corresponds to the front shown in figure 6(*a*). A vertical slice through the space–time plot would yield insight into the variation in time of the concentration at that particular location x. It is interesting to note that for certain locations x, this yields a brief temporal oscillation in the concentration. The peaks in the space–time plot correspond to the periodic formation of the cusp where the reaction is completed first. The time period of these peaks is $t \approx 0.8$. The periodic dynamics of the cooperative front is further illustrated in supplementary movie 2.

Figure 7(*b*) shows the space–time plot for the front with antagonistic feedback. The space–time plot indicates a sharper transition between the products and reactants. In addition, the right side of the reaction zone is not a linear feature as it was for cooperative feedback, it now forms an outline around the peaks containing products. This can be traced
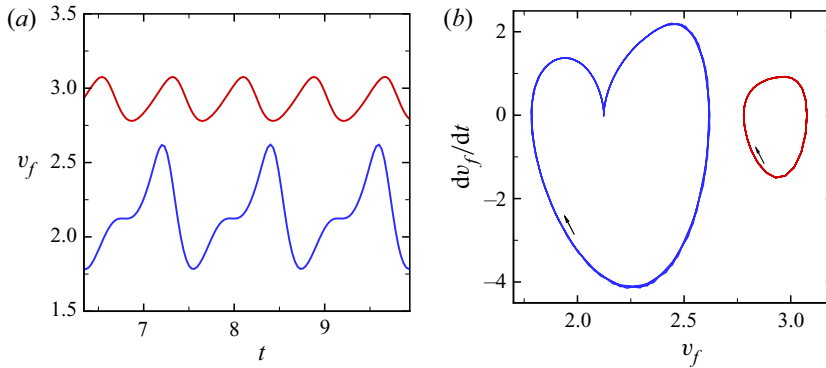
Figure 8. The time variation of the front velocity v_f for exothermic fronts with solutal feedback in a quiescent fluid. (*a*) The variation v_f with time t for cooperative feedback (upper curve, red) and antagonistic feedback (lower curve, blue). (*b*) The same data plotted as a phase portrait for cooperative feedback (right, red) and antagonistic feedback (left, blue). The direction in which the phase portrait is traversed is indicated by the arrows. Cooperative feedback: $Ra_T = 1000$, $Ra_s = 300$, $\eta = 50$. Antagonistic feedback: $Ra_T = 1000$, $Ra_s = -300$, $\eta = 50$.

to the lack of an extended leading edge for fronts with antagonistic feedback. The dashed line at $t = 5.97$ corresponds to the front shown in figure 6(*b*). Vertical slices at carefully chosen locations on the *x*-axis would yield the presence of brief temporal oscillations of the concentration during the transition from reactants to products. Overall, the space–time plot for antagonistic feedback is quite sharp and jagged due to the absence of a steady extended leading edge. The leading edge of the front, in this case, consists of dense products that descend into the bulk of the fluid layer from the region near the top plate. This event repeats in time as the chemical reaction continues generating products that form the leading edge. The leading edge rises due to heat release until it cools due to the top wall, which contributes to its eventual descent. The peaks of the products coincide with the falling of the leading edge of the front to the point where it reaches the mid-plane and is therefore shown on the space–time plot. The peaks also indicate the locations where the reaction is completed first. The peaks have a time period of $t \approx 1.2$, which is larger than the period of the dynamics for cooperative feedback. The periodic dynamics for fronts with antagonistic feedback is driven predominantly by the periodic dynamics of the dense leading edge, which is driven by the competition between the solutal and thermal feedback. The periodic dynamics of the antagonistic front is further illustrated in supplementary movie 2.

The periodicity of the dynamics can be illustrated further by plotting the front velocity as a function of time as shown in figure 8(*a*). The front velocity for the cooperative case is larger as a result of the combined effect of the solutal and thermal coupling. For the antagonistic case, the denser products of the reaction result in slowing down the front. However, it is important to note that the front velocity in the absence of solutal and thermal feedback is $v_0 = 0.6$, which illustrates the significant front enhancement caused by either cooperative or antagonistic coupling when compared with this baseline case.

For cooperative feedback, $v_f(t)$ is periodic with a single peak with a time period of $t \approx 0.8$. The single peak is due to the dynamic cusp structure, caused by the heat release, which creates regions of isolated reactants that are rapidly consumed. For antagonistic feedback, this process is significantly enhanced by the periodic turnover of the leading edge, which yields a periodic signal for v_f with two peaks. The turnover of the leading edge, in this case, significantly increases the amount of reactants in the isolated regions

942 A36-14

and results in the larger peak as the reactants are consumed. The smaller amplitude peak is due to the dynamics of the counter-rotating convection rolls and cusp structure and their role in the formation of the isolated regions of reactants. The time period of oscillation for antagonistic feedback is $t \approx 1.2$.

Figure 8(b) shows the phase portrait of the front velocity where we plot dv_f/dt vs v_f. The curve on the right (red) is for cooperative feedback where the unimodal oscillations of $v_f(t)$ result in an oval shaped closed curve. The curve includes three orbits to illustrate the periodic dynamics. The time span used is $6.84 \leq t \leq 9.24$. The closed curve on the left (blue) is for antagonistic feedback. The bimodal oscillation of $v_f(t)$ results in the two-lobed shape of the phase portrait. The pinched region, between the lobes, is due to the dynamics of the dense leading edge descending into the bulk of the flow field. The phase portraits clearly reflect that the front with cooperative feedback is faster than the front with antagonistic feedback. In addition, the cooperative front undergoes smaller magnitude oscillations in both dv_f/dt and v_f. This is because for the cooperative case, the leading edge is steady and the time varying dynamics is due to the cusp formed behind the front due to the heat release from the reaction. For antagonistic feedback, however, the motions of the leading edge of the front and the cusp region are periodic in time and both are evident in the phase portrait.

It is useful to compare the front velocities for several of the cases we have explored so far to quantify the front velocity enhancement due to the induced fluid motion from the solutal and thermal coupling. First, we note that the average front velocities for cooperative and antagonistic feedback are $\bar{v}_f = 2.92$ and $\bar{v}_f = 2.15$, respectively. In the absence of solutal feedback we found that the exothermic front had a velocity of $\bar{v}_f = 2.63$, as shown in figure 5(b), which is faster than the front with antagonistic feedback and slower than the front with cooperative feedback. This also suggests that for an exothermic front, cooperative feedback increases the front velocity whereas the antagonistic feedback reduces the front velocity.

3.3. *An exothermic front with solutal feedback propagating through a cellular flow field*
$$(Ra_T > Ra_{T,c}, \; Ra_s \neq 0, \; \eta > 0)$$

We next study an exothermic front with solutal feedback that is propagating through a cellular flow field generated by Rayleigh–Bénard convection. Prior to initiating the front, we establish a chain of counter-rotating convection rolls over the entire fluid layer by numerically integrating (2.1)–(2.3) with the supercritical Rayleigh number $Ra_T = 3000$ and $Ra_s = \eta = 0$. The cellular flow field is generated using hot sidewall boundary conditions such that $T(x = 0) = T(x = \Gamma) = 1$. This yields an upflow at the left and right sidewalls, which initiates the growth of convection rolls that eventually fill the fluid layer. For our domain with $\Gamma = 30$, this procedure yielded 15 pairs of time-independent counter-rotating convection rolls. The width of a single roll is approximately unity, as shown in figure 9. The characteristic fluid velocity of this field of convection rolls is $U = 11.29$. In determining U we do not include the region near the hot sidewalls and use the spatial region $5 \leq x \leq 25$. After establishing the cellular flow field, we initiate the front at the left wall, which then propagates to the right. We use this cellular flow field to study a front with cooperative feedback ($Ra_s = 300, \eta = 50$) and a front with antagonistic feedback ($Ra_s = -300, \eta = 50$).

Figure 10 shows fronts propagating through the cellular flow field where (a–c) are for a front with cooperative feedback and (d–f) are for a front with antagonistic feedback. Colour contours of $c(x, z, t)$ are shown with arrows representing fluid velocity vectors.

Figure 9. Counter-rotating convection rolls generated by Rayleigh–Bénard convection. This flow field is used to study fronts propagating though a cellular flow field. Colour contours are of the streamfunction, where red indicates counter-clockwise rotation and blue indicates clockwise rotation. The characteristic fluid velocity is $U = 11.29$. Simulation parameters: $\Gamma = 30$, $Ra_T = 3000$.
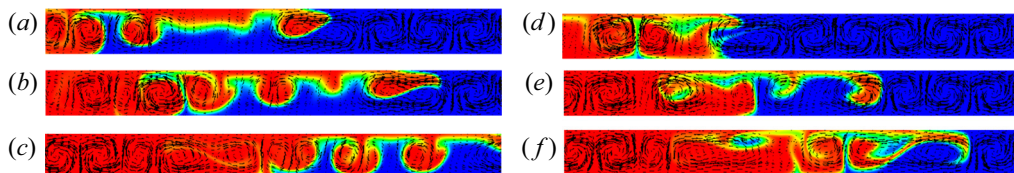

Figure 10. Exothermic fronts propagating through a cellular flow field generated by Rayleigh–Bénard convection. Colour contours of $c(x, z, t)$, where red is pure products and blue is pure reactants. Arrows are fluid velocity vectors. A close-up view is shown for $10 \leq x \leq 20$ to emphasize the front. (*a–c*) Cooperative feedback: $Ra_T = 3000$, $Ra_s = 300$, $\eta = 50$. (*d–f*) Antagonistic feedback: $Ra_T = 3000$, $Ra_s = -300$, $\eta = 50$. Panels (*a–c*) and (*d–f*) are separated by approximately 0.5 time units to illustrate the dynamics.

Figure 10(*a–c*) shows a front with cooperative feedback at three instances of time separated by approximately 0.5 time units, respectively. In figure 10(*a*), the cellular flow field is clearly evident in the velocity vectors of the pure reactants that are to the right of the front. The extended leading edge of the front is dynamic due to its interactions with the flow field. The leading edge is advected by the convection rolls during the front propagation. There are also smaller plumes composed of falling products that form behind the leading edge. These plumes result from the interactions of the heat release and the cellular flow to create disordered spatial structures. As the front advances, the cellular flow is temporarily annihilated by the clockwise rotating solutal roll coincident with the leading edge of the front. The cellular flow re-emerges behind the reaction zone after the front has passed. The re-established cellular flow is clearly evident at the far left of figure 10(*c*). There are also isolated patches of reactants (blue) that form between the plumes during the reaction.

Figure 10(*d–f*) shows the front with antagonistic feedback travelling through the cellular flow field, where each panel is separated in time by approximately 0.5 time units. In this case, the leading edge of the front consists of heavier products, which descend while scooping reactants that become surrounded by products. The leading edge of the front interacts with the cellular flow in a complicated way resulting in a spatially disordered structure with intricate features. The spatial extent of the leading edge is smaller than what was found for cooperative feedback. The front annihilates the cellular flow as it propagates while creating secondary cellular flow structures in its immediate wake. The cellular flow field of Rayleigh–Bénard convection re-emerges after the front passes through which can be seen on the far left of the fluid layer in figure 10(*f*).

Space–time plots of the fronts propagating through the cellular flow field are shown in figure 11 using the same conventions as figure 7. The solid (dashed) lines indicate the locations of the centre of the Rayleigh–Bénard convection rolls with clockwise (counter-clockwise) rotation before the front propagates through. The centre of a convection roll is identified as the x location where $T(z = 1/2) = 1/2$.

Figure 11(*a*) shows the space–time plot for a front with cooperative feedback propagating through a cellular flow field. The space–time plot is highly disordered with several interesting features. The islands of products along the reaction zone occur when the extended leading edge of the front crosses below the mid-plane. This crossing is due
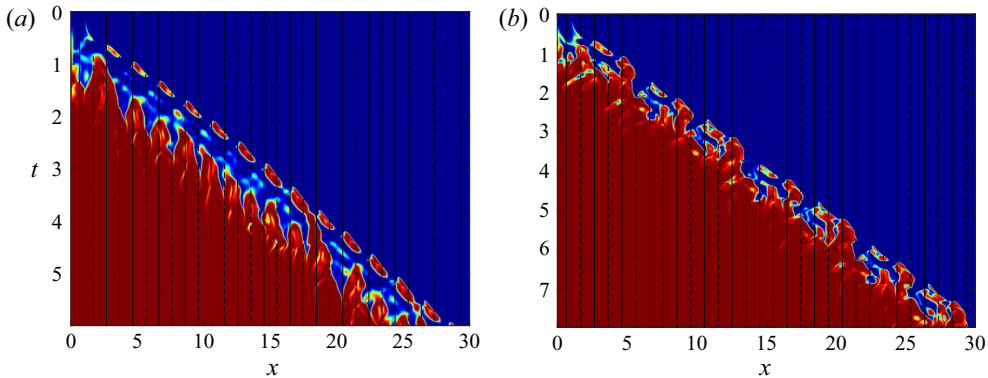
Figure 11. Space–time plots of fronts propagating through a cellular flow field. Colour contours are of $c(x, z = 1/2, t)$, where red is products and blue is reactants. The locations of the centres of the Rayleigh–Bénard convection rolls are indicated by a solid (dashed) line for rolls with clockwise (counter-clockwise) rotation. (*a*) Cooperative feedback: $\eta = 50$, $Ra_s = 300$, and $Ra_T = 3000$. Fronts are shown in figure 10(*a–c*). (*b*) Antagonistic feedback: $\eta = 50$, $Ra_s = -300$, and $Ra_T = 3000$. Fronts are shown in figure 10(*d–f*).

to the presence of a clockwise rotating convection roll, which advects the leading edge downwards even though the leading edge consists of lighter products. The leading edge is coincident with a clockwise rotating solutal roll as indicated in figure 10(*a–c*). This clockwise rotating roll becomes strengthened when it absorbs a clockwise rotating thermal convection roll. Similarly, it gets weakened when it absorbs a counter-clockwise rotating thermal convection roll. The islands of products represent the regions in the space–time plot where the reaction is first completed. These regions coincide with a clockwise rotating thermal convection roll pulling the leading edge downward to complete the reaction. This is evident from the space–time plot since these features predominantly occur on the right of the centres of the clockwise rotating rolls (solid lines).

The space–time plot for a front with antagonistic feedback that is propagating through the cellular flow field is shown in figure 11(*b*). In this case, the space–time plot is more disordered than what was found for cooperative feedback. The front with antagonistic feedback, in the absence of a cellular flow field, is coincident with a clockwise rotating convection roll at the leading edge as shown in figure 6(*b*). The clockwise thermal convection rolls strengthen this leading clockwise front-induced roll and helps to advance the front forward. This mechanism is similar to the dynamics found for a front with cooperative feedback in a cellular flow field. However, the leading edge in the antagonistic case is composed of denser products, which descends significantly trapping reactants in the process.

Although the dynamics shown in figure 11 contains features and structures that occur repeatedly in time, the dynamics is not periodic. This is evident from the space–time plots, where the disordered features such as fingers and isolated patches of products do not precisely repeat. It is apparent that the interactions of the front with the cellular flow field breaks the periodicity of the dynamics. This should be contrasted with fronts that propagate through a cellular flow field without heat release or solutal feedback which show a time-periodic dynamics (for example, see figure 12(*d*) in Mukherjee & Paul 2020). This indicates that the feedback between the reaction and the cellular flow field results in the aperiodic dynamics.

The variation of the front velocity with time for the cooperative and antagonistic fronts propagating though a cellular flow field is shown in figure 12(*a*). The upper
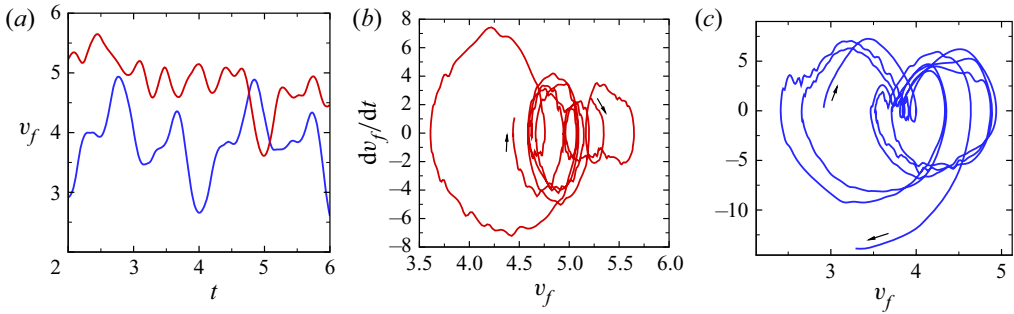
942 A36-17

Figure 12. (*a*) The variation of the front velocity with time for fronts propagating through a cellular flow field with cooperative feedback (red, upper) or antagonistic feedback (blue, lower). (*b*) The phase portrait for cooperative feedback for $2 \leq t \leq 6$. (*c*) The phase portrait for antagonistic feedback for $2 \leq t \leq 8$. Arrows indicate the direction of the trajectory. Cooperative feedback: $Ra_s = 300$, $Ra_T = 3000$, $\eta = 50$. Antagonistic feedback: $Ra_s = -300$, $Ra_T = 3000$, $\eta = 50$.

curve (red) is $v_f(t)$ with cooperative feedback and the lower curve (blue) is $v_f(t)$ with antagonistic feedback. The front velocity for cooperative feedback is faster than that of antagonistic feedback on average. It is evident that neither of the front velocities repeat in time.

The aperiodic nature of $v_f(t)$ is illustrated further by the phase portraits shown in figure 12(*b,c*). The direction in which the trajectory traverses the phase portrait is indicated by the arrows. The phase portrait for a front with cooperative feedback is shown in figure 12(*b*) and is quite disordered. The clockwise orbit of the trajectory reveals a noisy signature of the oval structure shown in figure 8(*b*) for a front with cooperative feedback propagating through an initially motionless fluid. For the front with antagonistic feedback, the trajectory also reveals a noisy signature of the orbit shown in figure 8(*b*). There is a two-lobed structure with a pinched region between the lobes due to the dynamics of the dense leading edge of the front. To explore if the dynamics ever settles to a periodic solution at long times, we performed a numerical simulation in a larger domain with an aspect ratio of $\Gamma = 60$. Even in this larger domain, the dynamics remained aperiodic for the duration of the front propagation. The interactions of the front with a cellular flow field leads to an aperiodic dynamics for both cooperative and antagonistic feedback. The intricate spatio-temporal dynamics of the cooperative and antagonistic fronts in the presence of background convection is further illustrated in supplementary movie 3.

In figure 13 we gather together the time-averaged diagnostics of the characteristic fluid velocity $\bar{U}$, front velocity $\bar{v}_f$ and the length of the reaction zone $\bar{L}_s$ for an exothermic front, $\eta = 50$, that is propagating through a two-dimensional fluid layer. Figure 13 presents a comparison of the results for fronts propagating through an initially motionless fluid, $Ra_T = 1000$, with fronts propagating through a cellular flow field, $Ra_T = 3000$. Fronts with cooperative coupling, $Ra_s = 300$, are squares (red) and fronts with antagonistic coupling, $Ra_s = -300$, are circles (blue). The error bars on the symbols indicate the standard deviation of the time varying values about the mean.

Figure 13(*a*) illustrates the variation of the characteristic fluid velocity. When the fluid layer is initially motionless, all fluid motion is due to the front, and it is evident that the fluid velocity induced by the front is larger for the case of cooperative coupling. However, for the case of cellular flow, the value of $\bar{U}$ is not significantly affected by the presence of the front or the type of coupling. This indicates that the characteristic fluid velocity is dominated by the cellular flow field for these conditions. We note that the characteristic
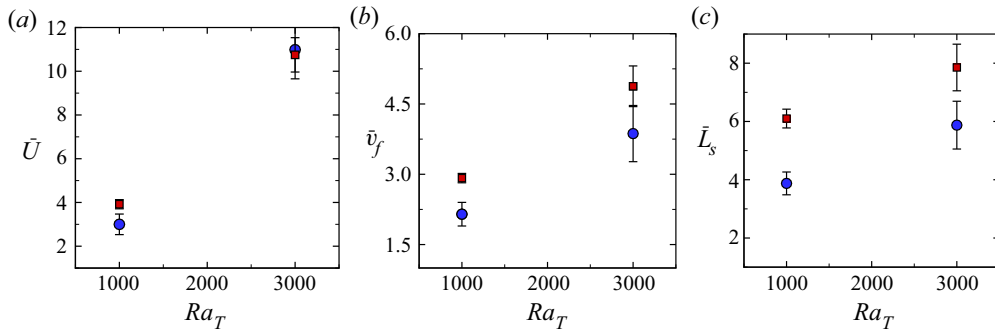
942 A36-18

Figure 13. A comparison of the time-averaged values of the (*a*) characteristic fluid velocity, (*b*) front velocity and (*c*) reaction zone length of an exothermic front with $\eta = 50$ travelling through a two-dimensional layer of fluid that is initially motionless ($Ra_T = 1000$) or contains a cellular flow field ($Ra_T = 3000$). Squares (red) are for cooperative coupling with $Ra_s = 300$, circles (blue) are for antagonistic coupling with $Ra_s = -300$. The error bars represent the magnitude of the standard deviation of the time variation about the mean value.

fluid velocity for the cellular flow, in the absence of the front, is $\bar{U} = 11.29$ as shown in figure 9.

The time-averaged values of the front velocities are plotted in figure 13(*b*). It is evident that the front with cooperative coupling is always faster than the front with antagonistic coupling. Furthermore, the fronts are significantly faster when propagating through the cellular flow field. The oscillations of $v_f(t)$ about the mean value $\bar{v}_f$ are larger for the case when the front propagates through the cellular flow field. This is due to the complex interactions between the front and the counter-rotating convection rolls of the cellular flow. Figure 13(*c*) shows the time average of the reaction zone length, or mixing length. The reaction zone length exhibits a similar trend to that of $\bar{v}_f$ where $\bar{L}_s$ is always larger for the front with cooperative feedback and $\bar{L}_s$ increases in the presence of a cellular flow field.

3.4. *Fronts travelling through a chaotic three-dimensional layer of fluid*

We now investigate an exothermic front that propagates through a three-dimensional convective flow field exhibiting spatio-temporal chaos generated by Rayleigh–Bénard convection. We use the cylindrical domain shown in figure 1(*b*) with an aspect ratio of $\Gamma = 40$ that contains a fluid with Prandtl number $Pr = 1$. The thermal Rayleigh number is set to $Ra_T = 6000$, which yields the state of spiral defect chaos (Morris *et al.* 1993). Spiral defect chaos consists of a dynamic pattern of convection rolls that contains many defect structures including spirals, targets and dislocations. Previous numerical investigations have explored the chaotic nature of this flow field in quantitative detail (cf. Paul *et al.* 2007; Karimi & Paul 2012). The flow field is chaotic as indicated by a positive leading Lyapunov exponent. We first integrate (2.1)–(2.3) for $t \approx \Gamma^2$ to allow for initial transients to decay and to establish the chaotic flow field. It is within this flow field that we initiate a front at the centre of the domain and then study its propagation outward toward the sidewall. The time-averaged value of the characteristic fluid velocity for these conditions is $\bar{U} = 28.63$, where $\bar{U}$ is computed at the mid-plane ($z = 1/2$) of the convection domain.

The scale of the computations for the three-dimensional study is significantly larger than for our investigation of fronts through a two-dimensional layer of fluid. The complexity of the front increases, and its thickness decreases, with decreasing values of the Lewis number. The necessity to resolve the small scale features of the front dominate the
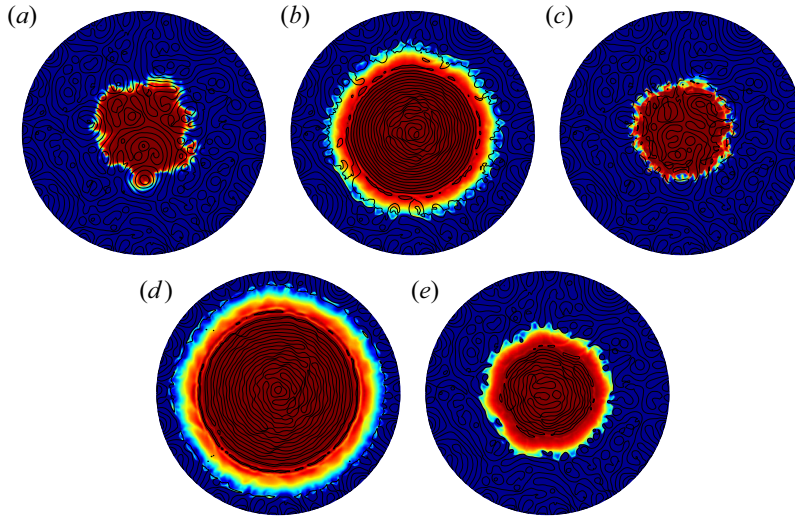
Figure 14. The propagation of a front through a three-dimensional chaotic flow field. The front is initiated at the centre at $t = 0$. Colour contours are shown of $c(x, y, z = 1/2, t)$ at $t = 3.4$, where red is products and blue is reactants. Black lines are contours of $T = 1/2$, indicating the location of the centre of the convection rolls. (*a*) Without solutal coupling and without heat release: $Ra_s = \eta = 0$. (*b*) Solutal coupling and without heat release: $Ra_s = 6000$, $\eta = 0$. (*c*) Without solutal coupling and with heat release: $Ra_s = 0$, $\eta = 18$. (*d*) Cooperative feedback: $Ra_s = 6000$, $\eta = 18$. (*e*) Antagonistic feedback: $Ra_s = -6000$, $\eta = 18$. In all panels: $Ra_T = 6000$, $Le = 0.1$.

calculation for these conditions, and we found that it was prohibitive to conduct the three-dimensional study using $Le = 0.01$. We found that it was possible to proceed with $Le = 0.1$. For the exothermic reaction we use $\eta = 18$, which yields a maximum temperature of the fluid layer of approximately unity. For the solutal Rayleigh number we use $Ra_s = 6000$ for cooperative feedback and $Ra_s = -6000$ for antagonistic coupling. This larger value of Ra_s is to ensure that the front-induced fluid velocity from the solutal coupling is comparable to the fluid velocity of the spiral defect chaos flow field. We initiate the front at the centre of the domain using a Gaussian initial condition for the radial variation of the initial concentration field.

Figure 14 illustrates fronts propagating through a chaotic flow field for the different conditions that we have quantified. In all panels, a mid-plane slice is shown at $z = 1/2$ with colour contours of the concentration where red is products and blue is reactants. The black solid lines are contours of the temperature at $T = 1/2$, which yields the location of the centre of the convection rolls. As a result, the black solid lines provide insight into the underlying pattern of convection rolls. The front is initiated at $t = 0$ and all panels show the front at $t = 3.4$. We emphasize that all fronts were initiated from the exact same initial flow field.

Figure 14(*a*) shows a front without solutal feedback and without heat release ($Ra_s = \eta = 0$). In this case without front-induced fluid motion, the chaotic fluid motion of Rayleigh–Beńard convection alters the front interface as it travels radially outward. The interactions with the chaotic flow field create small scale features, which wrinkle the front that effectively increases the surface area for the reaction to occur. A detailed study of fronts travelling through a chaotic flow field without solutal feedback and without heat release can be found in Mukherjee & Paul (2019). Figure 14(*a*) provides a useful baseline

case upon which to compare the fronts with more complex interactions that are shown in figure 14(*b–d*).

Figure 14(*b*) shows a front with solutal coupling and without heat release ($Ra_s = 6000$, $\eta = 0$). The solutal coupling yields a large solutally driven toroidal convection roll that encompasses the leading edge of the front and travels with the front. This results in an extended front interface, which provides a greater surface area for the reaction to occur. This is indicated by the prominent yellow/green ring around the front, which yields an increased front speed when compared with figure 14(*a*). The absence of black contour lines in the reaction zone indicate that the solutally driven convection roll has annihilated the Rayleigh–Bénard convection rolls that were present prior to the approach of the front. Behind the propagating front, the Rayleigh–Bénard convection rolls re-emerge in a target pattern of concentric convection rolls. This target pattern formed behind the front is unstable to spiral defect chaos, which is eventually reestablished for long times.

Figure 14(*c*) illustrates the front without solutal coupling and with heat release ($Ra_s = 0$, $\eta = 18$). In this case, the heat release from the reaction generates a pair of counter-rotating convection rolls that travel with the front. The heat release from the reaction, and the travelling pair of convection rolls, causes some distortion and annihilation of the Rayleigh–Bénard convection rolls that are present, which can be seen upon comparing with the black contour lines of figure 14(*a*). Behind the front, a chaotic fluid state is formed and there is no intermediate pattern of concentric rolls. The front velocity with heat release is slightly larger than the baseline front shown in figure 14(*a*). The reaction zone consists of fluid at a higher temperature than the surrounding fluid due to the heat release, which yields a jagged front interface. Overall, the front interface is more circular, on average, than the front of figure 14(*a*).

Figure 14(*d*) shows the front with cooperative feedback where $Ra_s = 6000$ and $\eta = 18$. It is useful to compare this result with the case of only solutal coupling shown in figure 14(*b*) and the case of only heat release shown in figure 14(*c*). It is clear that the solutally driven convection roll is present in figure 14(*d*) and that this roll annihilates the Rayleigh–Bénard convection rolls as the front propagates outward. Behind the front is a pattern of concentric rolls that eventually evolve to spiral defect chaos. Furthermore, the front velocity for figure 14(*d*) is larger than the front velocities for either figure 14(*b,c*). This indicates that the combined cooperative effect of the solutal coupling and the heat release contribute to an increased front velocity.

The front with antagonistic feedback is shown in figure 14(*e*) where $Ra_s = -6000$ and $\eta = 18$. The front has an extended leading edge due to the solutal coupling. However, the products are more dense than the reactants, which decreases the length of the reaction zone when compared with the cooperative case shown in figure 14(*d*). The front is followed by concentric convection rolls, which are formed by the solutal convection roll as it travels with the front. The front velocity with antagonistic coupling is less than the front velocity for the cooperative case shown in figure 14(*d*) and it is larger than the front velocity when only heat release is included as shown in figure 14(*c*). This supports the conclusion, for the parameters we have explored, that any induced fluid motion by the front will increase the front velocity, with respect to the front velocity v_0 in the absence of induced fluid motion, where a cooperative contribution is more effective than an antagonistic contribution.

The temperature of the fluid layer at mid-depth is shown in figure 15 for the fronts shown in figure 14. In figure 15, red is hot rising fluid ($T = 1$) and blue is cold descending fluid ($T = 0$). Figure 15(*a*) shows the temperature field without any influence of the front where the spiral defect chaos state of the fluid is evident. Figure 15(*b*) shows the fluid temperature field for a front without heat release and with solutal coupling. The large green/yellow ring is due to the solutal convection roll that is annihilating the Rayleigh–Bénard convection
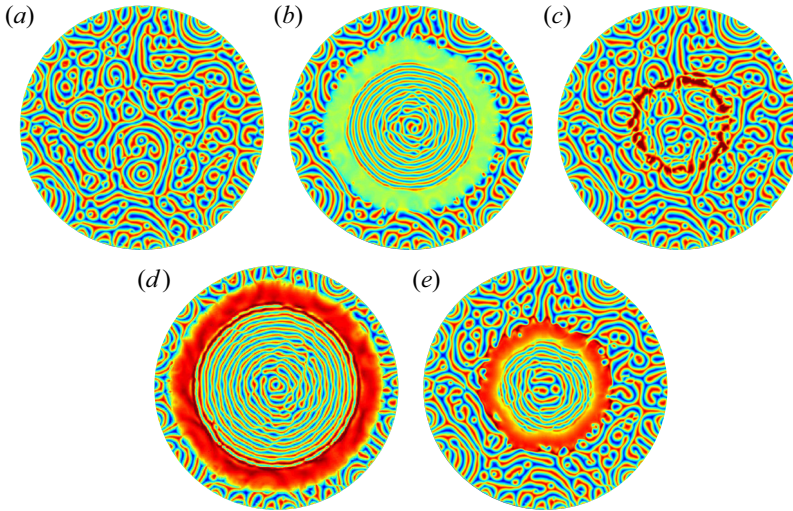
Figure 15. The fluid temperature of a chaotic flow field containing a propagating front. Red is hot rising fluid ($T = 1$) and blue is cold descending fluid ($T = 0$). (*a*) A front without solutal coupling and without heat release ($Ra_s = \eta = 0$). In this case, the temperature field is unaltered by the front and the state of spiral defect chaos is clearly evident. (*b*) A front with solutal coupling and without heat release ($Ra_s = 6000$, $\eta = 0$). (*c*) A front without solutal coupling and with heat release ($Ra_s = 6000$, $\eta = 18$). (*d*) A front with cooperative feedback ($Ra_s = 6000$, $\eta = 18$). (*e*) A front with antagonistic feedback ($Ra_s = 6000$, $\eta = 18$). In all panels $Ra_T = 6000$ and $Le = 0.1$.

rolls while travelling outward with the front. Since there is no heat release due to the reaction for this case, the temperature of the solutal roll at mid-depth is $T \approx 1/2$.

The temperature field for the front without solutal coupling and with heat release is shown in figure 15(*c*). The heat release from the reaction generates a ring of elevated temperatures that travel with the front. It is also clear that the heat release due to the reaction has altered the chaotic fluid motion in the reaction zone. The temperature field for the front with cooperative feedback is shown in figure 15(*d*). The large solutal convection roll travelling with the front is composed of warm fluid due to the heat release from the reaction. The temperature field for the front with antagonistic feedback is shown in figure 15(*e*). The solutal convection roll is composed of warm fluid due to the heat release from the reaction.

The flow field of a striped pattern with defects can be quantified effectively using the local wavenumber q, which can be computed using the approach of Egolf, Melnikov & Bodenschatz (1998). We compute the local wavenumber using the temperature variation shown in figure 15. This yields a value of q for every location in space at the mid-depth slice, which allows the quantification of how a pattern changes spatially. Figure 16 shows the spatial variation of q where colour contours are for $1 \le q \le 4$ where blue is small wavenumber and red is large wavenumber.

Figure 16(*a*) shows q when the front does not affect the flow field ($Ra_s = \eta = 0$). Therefore, this image shows the wavenumber variation for a flow field of spiral defect chaos. The wavenumber varies significantly over space with regions of small and large wavenumber associated with different topological feature of the flow field. The spatial average of the local wavenumber of this flow field is $\langle q \rangle = 2.36$.

Figure 16(*b*) shows q for a front with solutal coupling and without heat release. The large solutal convection roll yields the ring of small wavenumber (blue) that travels with the front. The concentric convection rolls that form behind the front are at large
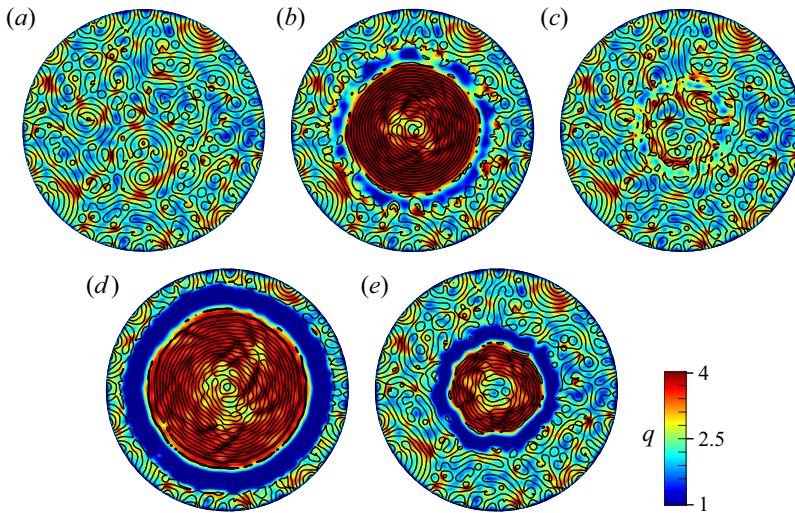
Figure 16. The spatial variation of the local wavenumber q of the fluid patterns. Colour contours are of q, where blue is small and red is large over the range $1 \leq q \leq 4$. (*a*) The spiral defect chaos flow field ($Ra_s = \eta = 0$). (*b*) A front with solutal coupling and without heat release ($Ra_s = 6000$, $\eta = 0$). (*c*) A front without solutal coupling and with heat release ($Ra_s = 0$, $\eta = 18$). (*d*) A front with cooperative feedback ($Ra_s = 6000$, $\eta = 18$). (*e*) A front with antagonistic feedback ($Ra_s = -6000$, $\eta = 18$). In all panels, $Ra_T = 6000$ and $Le = 0.1$.

wavenumber (red). The spatial average of the local wavenumber selected by the concentric rolls is $\langle q \rangle = 3.93$, which is significantly larger than the average wavenumber of the spiral defect chaos state. The instability of this transient field of concentric rolls is already evident by the deviations from a perfect target pattern. This large value of the wavenumber lies outside of the stability balloon at these conditions (Bodenschatz *et al.* 2000). Figure 16(*c*) shows q for a front without solutal coupling and with heat release. In this case, the spatial variation of q is less significant and $\langle q \rangle = 2.38$. The smaller effect of the heat release on the flow field pattern is evident by the ring of wavenumber values where $q \approx 2.5$ near the front. It would be interesting to explore the influence of the heat release on the fluid dynamics for larger values of the heat release parameter η. However, we have not explored this possibility further.

The variation of $\langle q \rangle$ for a front with cooperative and antagonistic feedback are shown in figure 16(*d,e*), respectively. It is clear that the solutally generated roll yields a ring of small wavenumber (blue) that travels with the front and annihilates Rayleigh–Bénard convection rolls as it progresses. Behind the front is a field of concentric convection rolls of high wavenumber (red).

Concentric rolls are formed behind the front only when solutal coupling is present for the parameter values we have explored as shown in figure 16(*b,d,e*). In these cases with solutal coupling, a clockwise rotating solutal convection roll (in the r–z plane) is formed that travels with the front. The leading edge of the solutal roll is a downflow, which interacts directly with the chaotic flow field that is ahead of the front. For our parameters, the leading edge of the solutal roll annihilates the chaotic flow field. The trailing edge of the solutal roll is an upflow. This upflow initiates the formation of Rayleigh–Bénard convection rolls since $Ra_T > Ra_{T,c}$. The azimuthal symmetry of the upflow causes these convection rolls to emerge as concentric rolls. The concentric convection rolls are also unstable, which leads to the fluid returning to a state of spiral defect chaos. At the instant of time shown in figure 16, the concentric rolls exhibit signs of instability as they evolve back toward the state of spiral defect chaos. It is interesting to note that the wavenumber of the concentric

rolls behind the front does not vary significantly for the three cases we explored with solutal coupling.

The concentric convection rolls are formed behind a moving upflow that is travelling with the front with velocity v_f. The average wavenumber of the concentric rolls is approximately 1.5 times larger than the wavenumber of the spiral defect chaos state. We highlight that the wavenumber selected by the concentric rolls behind the front $\langle q \rangle \approx 3.75$ is smaller than the wavenumber of maximum linear growth $\langle q \rangle \approx 5.04$ (Dominguez-Lerma, Ahlers & Cannell 1984) and larger than the wavenumber selected by a target pattern $\langle q \rangle \approx 2.8$ (Buell & Catton 1986). The wavenumber selection of this complex pattern forming front would be interesting to explore in more detail.

4. Conclusion

We have used high-order numerical simulations to quantify the front and fluid dynamics of a layer of reacting fluid over a broad range of conditions with a focus upon the different types of physical coupling that may be present. We have presented a careful study that built up in complexity from an initially motionless two-dimensional layer of fluid with a propagating front to a three-dimensional chaotic layer of fluid with a fully coupled front containing solutal and thermal contributions. Our intention was to choose parameter values to gain physical insights into the complex fluid, chemical and thermal interactions that are present as opposed to an exhaustive study, which is well beyond reach. Our numerical approach has allowed us to probe the complex dynamics of propagating fronts in a fluid in a regime where many fundamental theoretical questions remain and at a level of quantitative detail that is currently not possible experimentally.

We have shown that the fluid-induced motion of a front depends significantly upon the type of coupling that is present. For solutal coupling, a large solutal convection roll is formed and for a reaction with heat release a pair of counter-rotating convection rolls is generated. These front-induced fluid structures travel with the front. When both coupling mechanisms are present, the fluid-induced structure is a nonlinear combination of these contributions. The resulting fluid structure that travels with the front interacts in a complex way with an externally generated flow field if present. We studied this for a cellular flow field in two dimensions and for a chaotic flow field in three dimensions. The nonlinear interactions with the flow leads to a very complicated dynamics that includes aperiodic spatio-temporal features.

A physical understanding of these fundamental contributions to the front and fluid dynamics will be useful on several levels. The identification of the important features will guide the development of the theoretical ideas necessary to describe the complex and nonlinear dynamics of front propagation in a fluid. Our results also suggest that it may be possible to control a complex flow field by the presence of a reaction located at a favourable location in space. Control in this sense could be the generation of a transient pattern of concentric rolls or by briefly quenching chaotic fluid dynamics using a propagating front.

Author ORCIDs.

ⓘ S. Mukherjee https://orcid.org/0000-0003-2981-7383;

ⓘ M.R. Paul https://orcid.org/0000-0002-0701-1955.

REFERENCES

ABEL, M., CELANI, A., VERGNI, D. & VULPIANI, A. 2001 Front propagation in laminar flows. *Phys. Rev. E* **64** (4), 046307.

ABEL, M., CENCINI, M., VERGNI, D. & VULPIANI, A. 2002 Front speed enhancement in cellular flows. *Chaos* **12** (2), 481–488.

BARGTEIL, D. & SOLOMON, T.H. 2012 Barriers to front propagation in ordered and disordered vortex flows. *Chaos* **22**, 037103.

BODENSCHATZ, E., PESCH, W. & AHLERS, G. 2000 Recent developments in Rayleigh–Bénard convection. *Annu. Rev. Fluid Mech.* **32** (1), 709–778.

BUDRONI, M.A., RONGY, L. & DE WIT, A. 2012 Dynamics due to combined buoyancy – and Marangoni-driven convective flows around autocatalytic fronts. *Phys. Chem. Chem. Phys.* **14**, 14619–14629.

BUDRONI, M.A., UPADHYAY, V. & RONGY, L. 2019 Making a simple $a + b \rightarrow c$ reaction oscillate by coupling to hydrodynamic effect. *Phys. Rev. Lett.* **122**, 244502.

BUELL, J.C. & CATTON, I. 1986 Wavenumber selection in large-amplitude axisymmetric convection. *Phys. Fluids* **29**, 23–30.

CHANDRASEKHAR, S. 1961 *Hydrodynamic and Hydromagnetic Stability*. Dover.

CHIAM, K.-H., PAUL, M.R., CROSS, M.C. & GREENSIDE, H.S. 2003 Mean flow and spiral defect chaos in Rayleigh–Bénard convection. *Phys. Rev. E* **67**, 056206.

CONSTANTIN, P., KISELEV, A., OBERMAN, A. & RYZHIK, L. 2000 Bulk burning rate in passive-reactive diffusion. *Arch. Rat. Mech. Anal.* **154**, 53–91.

DEVILLE, M.O., FISCHER, P.F. & MUND, E.H. 2002 *High-Order Methods for Incompressible Fluid Flow*. Cambridge University Press.

DE WIT, A. 2020 Chemo-hydrodynamic patterns and instabilities. *Annu. Rev. Fluid Mech.* **52**, 531–555.

D'HERNONCOURT, J., ZEBIB, A. & DE WIT, A. 2007 On the classification of buoyancy-driven chemo-hydrodynamic instabilities of chemical fronts. *Chaos* **17** (1), 013109.

DOMINGUEZ-LERMA, M.A., AHLERS, G. & CANNELL, D.S. 1984 Marginal stability curve and linear growth rate for rotating Couette–Taylor flow and Rayleigh–Bénard convection. *Phys. Fluids* **27** (4), 856–860.

EGOLF, D.A., MELNIKOV, I.V. & BODENSCHATZ, E. 1998 Importance of local pattern properties in spiral defect chaos. *Phys. Rev. Lett.* **80**, 3228–3231.

FIELD, R.J. & BURGER, M. 1985 *Oscillations and Traveling Waves in Chemical Systems*. Wiley.

FISCHER, P.F. 1997 An overlapping Schwarz method for spectral element solution of the incompressible Navier–Stokes equations. *J. Comput. Phys.* **133**, 84–101.

FISHER, R.A. 1937 The wave of advance of advantageous genes. *Proc. Annu. Symp. Eugen. Soc.* **7**, 355–369.

HARGROVE, W.W., GARDNER, R.H., TURNER, M.G., ROMME, W.H. & DESPAIN, D.G. 2000 Simulating fire patterns in heterogeneous landscapes. *Ecol. Model.* **135** (2–3), 243–263.

JACOBSON, M.Z. 1999 *Fundamentals of Atmospheric Modeling*. Cambridge University Press.

JARRIGE, N., BOU MALHAM, I., MARTIN, J., RAKOTOMALALA, N., SALIN, D. & TALON, L. 2010 Numerical simulations of a buoyant autocatalytic reaction front in tilted Hele-Shaw cells. *Phys. Rev. E* **81**, 066311.

KARIMI, A. & PAUL, M.R. 2012 Quantifying spatiotemporal chaos in Rayleigh–Bénard convection. *Phys. Rev. E* **85**, 046201.

KOLMOGOROV, A.N., PETROVSKII, I.G. & PISKUNOV, N.S. 1937 A study of the equation of diffusion with increase in the quantity of matter, and its application to a biological problem. *Bull. Moscow Univ. Math.* **1**, 1–25.

MASERE, J., VASQUEZ, D.A., EDWARDS, B.F., WILDER, J.W. & SHOWALTER, K. 1994 Nonaxisymmetric and axisymmetric convection in propagating reaction-diffusion fronts. *J. Phys. Chem.* **98**, 6505–6508.

MEHRVARZI, C.O. & PAUL, M.R. 2014 Front propagation in a chaotic flow field. *Phys. Rev. E* **90**, 012905.

MORRIS, S.W., BODENSCHATZ, E., CANNELL, D.S. & AHLERS, G. 1993 Spiral defect chaos in large aspect ratio Rayleigh–Bénard convection. *Phys. Rev. Lett.* **71** (13), 2026–2029.

MUKHERJEE, S. 2020 Front propagation and feedback in convective flow fields. PhD thesis, Virginia Tech.

MUKHERJEE, S. & PAUL, M.R. 2019 Velocity and geometry of propagating fronts in complex convective flow fields. *Phys. Rev. E* **99**, 012213.

MUKHERJEE, S. & PAUL, M.R. 2020 Propagating fronts in fluids with solutal feedback. *Phys. Rev. E* **101**, 032214.

NAGYPAL, I., BAZSA, G. & EPSTEIN, I.R. 1986 Gravity-induced anisotropies in chemical waves. *J. Am. Chem. Soc.* **108** (13), 3635–3640.

NEVINS, T.D. & KELLEY, D.H. 2016 Optimal stretching in advection-reaction-diffusion systems. *Phys. Rev. Lett.* **117** (16), 164502.

NUGENT, C.R., QUARLES, W.M. & SOLOMON, T.H. 2004 Experimental studies of pattern formation in a reaction-advection-diffusion system. *Phys. Rev. Lett.* **93** (21), 218301.

PAUL, M.R., EINARSSON, M.I., FISCHER, P.F. & CROSS, M.C. 2007 Extensive chaos in Rayleigh–Bénard convection. *Phys. Rev.* E **75**, 045203.

POCHEAU, A. & HARAMBAT, F. 2008 Front propagation in a laminar cellular flow: shapes, velocities, and least time criterion. *Phys. Rev.* E **77**, 036304.

POJMAN, J.A. & EPSTEIN, I.R. 1990 Convective effects on chemical waves. 1. Mechanisms and stability criteria. *J. Phys. Chem.* **94**, 4966–4972.

POJMAN, J.A., EPSTEIN, I.R., MCMANUS, T.J. & SHOWALTER, K. 1991*a* Convective effects on chemical waves. 2. Simple convection in the iodate-arsenous acid system. *J. Phys. Chem.* **95**, 1299–1306.

POJMAN, J.A., NAGY, I.P. & EPSTEIN, I.R. 1991*b* Convective effects on chemical waves. 3. Multicomponent convection in the iron(II)-nitric acid system. *J. Phys. Chem.* **95**, 1306–1311.

POMEAU, Y. 2004 Diffusion and reaction-diffusion in fast cellular flows. *Chaos* **14** (3), 903–909.

RONGY, L. & DE WIT, A. 2009 Buoyancy-driven convection around exothermic autocatalytic chemical fronts traveling horizontally in covered thin solution layers. *J. Chem. Phys.* **131**, 184701.

RONGY, L., GOYAL, N., MEIBURG, E. & DE WIT, A. 2007 Buoyancy-driven convection around chemical fronts traveling in covered horizontal solution layers. *J. Chem. Phys.* **127** (11), 114710.

RONGY, L., SCHUSZTER, G., SINKÓ, Z., TÓTH, T., HORVÁTH, D., TÓTH, A. & DE WIT, A. 2009 Influence of thermal effects on buoyancy-driven convection around autocatalytic chemical fronts propagating horizontally. *Chaos* **19** (2), 023110.

RUSSELL, C.A., SMITH, D.A., WALLER, L.A., CHILDS, J.E. & REAL, L.A. 2004 *A priori* prediction of disease invasion dynamics in a novel environment. *Proc. R. Soc. Lond.* B **271**, 21–25.

VAN SAARLOOS, W. 2003 Front propagation into unstable states. *Phys. Rep.* **386**, 29–222.

SCHWARTZ, M.E. & SOLOMON, T.H. 2008 Chemical reaction fronts in ordered and disordered cellular flows with opposing winds. *Phys. Rev. Lett.* **100**, 028302.

SREENIVASAN, K.R., RAMSHANKAR, R. & MENEVEAU, C. 1989 Mixing, entrainment, and fractal dimensions of surfaces in turbulent flows. *Proc. R. Soc. Lond.* A **421**, 79–108.

TIANI, R., DE WIT, A. & RONGY, L. 2018 Surface tension- and buoyancy-driven flows across horizontally propagating chemical fronts. *Adv. Colloid Interface Sci.* **225**, 76–83.

VASQUEZ, D.A., LITTLEY, J.M., WILDER, J.W. & EDWARDS, B.F. 1994 Convection in chemical waves. *Phys. Rev.* E **50** (1), 280–284.

WILLIAMS, F.A. 1985 *Combustion Theory*. Benjamin-Cummings.

WU, Y., VASQUEZ, D.A., EDWARDS, B.F. & WILDER, J.W. 1995 Convective chemical-wave propagation in the Belousov-Zhabotinsky reaction. *Phys. Rev.* E **51**, 1119–1127.

XIN, J. 2000 Front propagation in heterogeneous media. *SIAM Rev.* **42** (2), 161–230.